### Propagation-Distance Limit for a Classical Nonlocal Optical System

Salman Sajad Wani, Xiaoping Shi, Saif Al-Kuwari, Arshid Shabir, and Mir Faizal, 4,5

<sup>1</sup> Qatar Center for Quantum Computing, College of Science and Engineering, Hamad Bin Khalifa University, Doha, Qatar <sup>2</sup> Irving K. Barber School of Arts and Sciences, University of British Columbia Okanagan, Kelowna, BC V1V 1V7, Canada <sup>3</sup>Canadian Quantum Research Center, 204-3002 32 Ave, Vernon, BC V1T 2L7, Canada <sup>4</sup>Department of Mathematical Sciences, Durham University,

Upper Mountjoy, Stockton Road, Durham DH1 3LE, UK <sup>5</sup> Faculty of Sciences, Hasselt University, Agoralaan Gebouw D, Diepenbeek, 3590 Belgium

We derive closed-form analog quantum-speed-limit (QSL) bounds for highly nonlocal optical beams whose paraxial propagation is mapped to a reversed (inverted) harmonic-oscillator generator. Treating the longitudinal coordinate z as an evolution parameter (propagation distance), we construct the propagator, evaluate the Bures distance, and obtain analytic Mandelstam-Tamm and Margolus-Levitin bounds that fix a propagation distance limit 2PDL to reach a prescribed mode

distinguishability. This distance-domain constraint is the classical optical analogue of the minimalorthogonality time in quantum mechanics. We then propose a compact self-defocusing PDL beam shaper that achieves strong transverse mode conversion within millimetre scales. We further show that small variations in refractive index, beam power, or temperature shift  $z_{\rm NL}$  with high leverage, enabling SL-based metrology with index sensitivities down to  $10^{-7}$  RIU and temperature resolutions of order 1 mK. The results bridge distance-domain QSL geometry and practical photonic applications.

#### I. INTRODUCTION

Quantum-speed limits (SLs) quantify the minimal time required for a physical state to evolve into an orthogonal configuration [1]. The canonical Mandelstam-Tamm (MT) bound links this analogue time to the energy variance  $\Delta E$  of the system, whereas the Margolus-Levitin (ML) bound relates it to the mean energy  $\langle E \rangle$  [2–4]. Together these results reveal that both energy dispersion and average energy constrain dynamical evolution, influencing the ultimate rates of quantum computation [5], metrology [6], and thermodynamic processes [7, 8]. SLs thus illuminate the interplay between energy, time, and uncertainty at a fundamental level, a connection further explored in optimal-control and open-system scenarios [9, 10].

Quantum theory, however, incorporates two distinct ingredients: unitary wave-like propagation governed by Schrödinger dynamics and the nonunitary measurement postulate. While the latter resists any classical analogue its incompatibility with local realism is established by Bell, Leggett, and Leggett-Garg inequalities [11–15] the former can be emulated in suitably engineered classical media. Recent work shows that SLs survive this quantum-to-classical translation: they hold for stochastic processes, Hamiltonian flows, open classical dynamics, and relativistic field theories, underscoring their universality [16–19].

Nonlocal optical platforms provide an especially transparent arena for such analogies. In these systems a slowly varying envelope A(X,Z) obeys a paraxial equation in which the longitudinal coordinate Z plays the role of analogue time t. When the medium exhibits a defocusing nonlocal response the induced refractive index profile forms an inverted parabola, mapping the beam dynamics to those of a quantum reverse harmonic oscillator

(RHO) [20, 21]. Consequently classical light can reproduce phenomena usually regarded as quantum, including tunnelling [22], superfluid-like flow [23], entanglement analogues [24], and harmonic-oscillator behaviour [25]. Because SLs depend solely on wave propagation, not on measurement collapse, they remain valid in this classical context. Below we exploit the RHO correspondence to derive MT and ML bounds for nonlocal optical beams, demonstrate their sharpness via numerical simulation. and propose applications in ultrafast beam shaping, optical switching, and high-resolution sensing.

We use the geometric QSL framework (Fubini-Study/Bures) for pure states under a z-independent generator: the Bures angle  $\mathcal{L}(z) = \arccos |F(z)|$  measures distance in projective Hilbert space, and the MT/ML bounds set lower limits on the required propagation distance [26]. This approach aligns with recent work that tightens and generalizes QSL bounds across many dynamics [27, 28] and shows that speed limits also govern classical stochastic and Hamiltonian systems [16– 18]. In our platform, paraxial propagation on  $L^2(\mathbb{R})$  is linear and norm-preserving-single-mode squeezing generated by the reversed harmonic oscillator-so the closedsystem MT/ML bounds are the relevant distance-domain QSLs for  $\psi$ . We derive explicit formulas for  $\langle H \rangle$  and  $\Delta H$  in terms of  $(\gamma, x_0, p_0)$  and compute the exact overlap F(z); together these give analogues of ML and MT bounds, we have  $z_{MT} \geq \mathcal{L}/\Delta H$ ,  $z_{ML} \geq \mathcal{L}/|\langle H \rangle|$ , and  $z_{PDL} = \max\{z_{MT}, z_{ML}\}$ . If loss or gain makes the evolution nonunitary, we switch to the open-system QSL framework: our distance-to-orthogonality statements then map to the unified bounds for arbitrary (in-

<sup>&</sup>lt;sup>1</sup> See Secs. II-III for the paraxial Schrödinger mapping and unitary  $L^2$  evolution.

cluding mixed) initial states of Zhang et al. [29].

#### II. ANALOGUE SCHRÖDINGER EQUATION

A linearly-polarized paraxial beam A(X,Z) in a nonlinear, nonlocal medium experiences an intensity-dependent index shift

$$n = n_0 + \Delta n(|A|^2), \tag{1}$$

where  $\Delta n$  is generally an integral of the surrounding intensity profile [30, 31]. Under the paraxial approximation the envelope obeys

$$i k \frac{\partial A}{\partial Z} = -\frac{1}{2k} \frac{\partial^2 A}{\partial X^2} - 2k \frac{\Delta n}{n_0} A,$$
 (2)

with  $k=2\pi n_0/\lambda_0$ . Introducing scaled variables  $x=X/X_0, z=Z/Z_0, \psi=A/A_0$  and assuming a defocusing nonlinearity

$$\Delta n = -\eta |A|^2, \qquad \eta > 0, \tag{3}$$

the nonlocal response can approximate a negative parabolic profile, yielding the inverted-oscillator Schrödinger analogue

$$i\frac{\partial\psi}{\partial z} = -\frac{\partial^2\psi}{\partial x^2} - \frac{\gamma^2}{2}x^2\psi,\tag{4}$$

where  $\gamma$  encodes the curvature of the effective potential [21, 22].

For comparison, the quantum harmonic oscillator Hamiltonian

$$\hat{H}_{\text{HO}} = \frac{\hat{p}^2}{2m} + \frac{1}{2}m\omega^2 \hat{x}^2 \tag{5}$$

has real discrete spectrum, whereas replacing the confining term by its negative produces the reverse harmonic oscillator (RHO)

$$\hat{H} = \frac{\hat{p}^2}{2m} - \frac{1}{2}m\omega^2 \hat{x}^2,\tag{6}$$

whose eigenvalues are complex and correspond to Gamow resonances [32, 33]. In the optical analogue, z takes the role of time, so the beam undergoes exponential transverse expansion analogous to a particle rolling down an inverted potential.

Because our analysis concerns only coherent wave propagation no measurement-induced collapse constraints from Bell-type, Leggett, or Leggett-Garg inequalities [11–15] are irrelevant: those inequalities restrict models of realism, not the Schrödinger dynamics itself. Consequently the same mathematical structure that underlies speed limits applies directly to nonlocal classical optics [16–19].

Experimentally, inverted parabolic index profiles arise in photorefractive or thermal media where a broad,

smoothed  $\Delta n$  acts as a negative lens; over finite propagation ranges the beam exhibits the predicted runaway broadening, providing a classical simulator of unstable quantum evolution. Thus Eq. (4) furnishes a rigorous foundation for applying quantum-inspired dynamical bounds, including speed limits, to classical nonlocal optical systems.

## III. EVOLUTION OPERATOR IN THE NONLOCAL OPTICAL SYSTEM

A monochromatic paraxial field  $\psi(x,z)$  evolving in a nonlocal, defocusing medium satisfies

$$i\frac{\partial}{\partial z}\psi(x,z) = \hat{H}\psi(x,z),$$
 (7)

with the inverted-oscillator Hamiltonian

$$\hat{H} = -\frac{\partial^2}{\partial x^2} - \frac{1}{2}\gamma^2 x^2. \tag{8}$$

Equation (7) is formally identical to a Schrödinger equation once the propagation coordinate z is regarded as "analogue time."

In this work z denotes propagation distance, not the laboratory time t. Our use of "time" is strictly analogue: by the paraxial Schrödinger correspondence  $i \partial_z \psi = \hat{H} \psi$ , z serves as an evolution (ordering) parameter that is mathematically isomorphic to time in quantum dynamics.

Although the potential is unbounded below, recent analyses show that propagation distance limit (PDL) bounds extend to such non-Hermitian generators provided the evolution is linear in a Hilbert space with the standard  $L^2$  inner product [28, 34]. The propagator is therefore

$$U(z) = \exp[-i\hat{H}z], \qquad \psi(x,z) = U(z)\psi(x,0),$$
 (9)

and an initial wave packet can be expanded as

$$\psi(x,z) = \sum_{n} c_n e^{-iE_n z} \phi_n^G(x),$$
 (10)

where the  $\phi_n^G$  are Gamow resonances of the RHO with complex  $E_n$ .

Introducing

$$\hat{u} = \frac{\gamma \hat{x} - \hat{p}}{\sqrt{2\gamma}}, \qquad \hat{v} = \frac{\gamma \hat{x} + \hat{p}}{\sqrt{2\gamma}}, \qquad \hat{a} = \frac{\hat{u} + i\hat{v}}{\sqrt{2}},$$
 (11)

and  $\hat{a}^{\dagger}$  as its adjoint, one finds  $\hat{H} = \frac{i}{2}(\hat{a}^2 - \hat{a}^{\dagger 2})$ , so that

$$U(z) = \exp[-i\hat{H}z] = \hat{S}(\xi) = \exp\left[\frac{1}{2}\left(\xi^* \hat{a}^2 - \xi \, \hat{a}^{\dagger \, 2}\right)\right], \, \xi = \gamma z \tag{12}$$

the standard squeezing operator, confirming the optical-quantum analogy.

For coordinate space calculations it is convenient to employ the factorization [35–37]

$$U(z) = (\cosh z)^{-1/2} \exp\left[\frac{i}{2}\tanh z \, x^2\right] \exp\left[-\ln\cosh z \, x \partial_x\right]$$
$$\exp\left[\frac{i}{2}\tanh z \, \partial_x^2\right]. \tag{13}$$

Applying (13) to a Gaussian input

$$\psi(x,0) = \left(\frac{1}{\pi}\right)^{1/4} \exp\left[-\frac{1}{2}x^2 + \sqrt{2}ax - \frac{1}{4}(a+a^*)^2\right], (14)$$

yields, in units with  $m = \omega = 1$ ,

$$\psi(x,z) = \left(\frac{1}{\pi}\right)^{1/4} (\cosh z)^{-1/2} \exp\left[i\frac{\tanh z}{2}x^2\right]$$

$$\exp\left[-\frac{\left(x/\cosh z - \sqrt{2}a\right)^2}{2\sigma^2(z)}\right],$$

$$\sigma^2(z) = \frac{1}{2}\left[1 + i\tanh z\right]. \tag{15}$$

Thus an initially narrow beam "explodes" transversely, mirroring the exponential divergence of RHO trajectories; the squeezing formalism captures both the amplitude scaling and the quadratic phase acquired during propagation.

Because the evolution is linear and the  $L^2$  norm is preserved, fidelities  $F(z) = \langle \psi(x,0) | \psi(x,z) \rangle$  and Bures angles can be defined exactly as in quantum theory. Consequently, Mandelstam-Tamm and Margolus-Levitin SL bounds apply unchanged once t is replaced by z, permitting rigorous time-distance limits in classical nonlocal optics even though no quantum measurement is involved. The inverted potential thereby provides an experimentally accessible platform for testing universal dynamical constraints derived for both quantum and classical waves.

## IV. PROPAGATION DISTANCE LIMIT IN THE OPTICAL SYSTEMS

With a real, lossless, highly nonlocal index profile,  $\hat{H} = \frac{1}{2}(\hat{p}^2 - \gamma^2 \hat{x}^2)$  is self-adjoint on  $L^2(\mathbb{R})$ , and  $U(z) = e^{-i\hat{H}z}$  is unitary (single-mode squeezing). Spectrally, the squeeze operator is unitary and has a purely continuous spectrum on  $L^2$  (no normalizable eigenvectors), so we define  $\langle H \rangle$  and  $\Delta H$  using the spectral theorem on  $\mathrm{Dom}(H)$  and  $\mathrm{Dom}(H^2)$  [38]. At this dynamical level, we derive and use the MT/ML distance-domain bounds [26].

The same quadratic dynamics also has a resonant representation in a rigged Hilbert space  $\Phi \subset L^2 \subset \Phi^{\times}$ , yielding Gamow (resonant) vectors with complex spectra and a one-sided semigroup for the resonant sector (time-asymmetric evolution). This provides an effective non-Hermitian picture of resonances that explains exponential reshaping and irreversibility in nonlocal media, while leaving the underlying unitary  $L^2$  evolution used for our QSLs unchanged [38, 39]. We use this language

only for modal interpretation (Sec. V); all QSL derivations are carried out on  $L^2$ .

If loss, gain, or reservoir coupling makes the evolution nonunitary, we apply open-system QSLs formulated for completely positive dynamical maps. Zhang et al. derive unified MT/ML-type lower bounds, expressed via relative purity and singular values of the generator, that apply to arbitrary initial states and generic nonunitary evolution [29]. Related open-system QSLs based on quantum Fisher information and Schatten norms give similar constraints [40–42]. In the unitary, pure-state, time-independent limit, these open-system bounds reduce to the closed-system MT form we use here. Conversely, to move to the open setting, replace the unitary distance with the contractive metric used in the nonunitary theory.

A pure optical state is the normalized field  $\psi(x, z)$ ; its fidelity with the initial profile is  $F(z) = \langle \psi(x, 0) | \psi(x, z) \rangle$ . The corresponding Bures (projective) angle [26]

$$\mathcal{L}(z) = \arccos|F(z)|,\tag{16}$$

is obtained explicitly from

$$F(z) = -1 + \operatorname{sech} z \left[ 1 + C(z) + D(z) \right], \tag{17a}$$

$$A(z) = -\operatorname{Im} a^2 - 2 \operatorname{Re} a^2,$$
 (17b)

$$E(z) = \frac{\operatorname{sech}^{-3/2} z}{\sqrt{H(z) \left[ 4 \cosh z + 4e^{-iz} - 2i \sinh z \right]}}, \quad (17c)$$

together with the auxiliary functions

$$f_{\pm}(z) = \pm 1 \mp \cosh(2z) + 3i \sinh(2z),$$
 (18a)

$$g(z) = \frac{(2 + \cosh(2z))\operatorname{sech}(z)}{e^{iz}},$$
(18b)

$$h(z) = \frac{(1 + i \tanh(z))(\sinh(2z) - i[5 + 3\cosh(2z)])}{\tanh(z) - i},$$
(18c)

$$G(z) = (5 + 3\cosh(2z) + i\sinh(z))(1 + i\tanh(z)),$$
(18d)

$$H(z) = \frac{e^{6\operatorname{Im}(a)^2}\cosh(z)}{e^{4\operatorname{Im}(a)^2} - 1 + \operatorname{sech}^2(z)} + i\sinh(z).$$
 (18e)

Substituting (16) yields the full analytic form of  $\mathcal{L}(z)$  identical to the longer expression previously given.

Expectation values with the (formally non-Hermitian)  $\hat{H}$  remain well defined for normalizable packets,

$$\langle H \rangle = \omega |a|^2 |\cos 2\theta|, \qquad \Delta H = \omega \sqrt{\frac{1}{2} + |a|^2}, \qquad (19)$$

so the Mandelstam-Tamm and Margolus-Levitin bounds translate to the optical domain as

$$z_{MT} \ge \frac{\mathcal{L}(z)}{\Delta H}, \qquad z_{ML} \ge \frac{\mathcal{L}(z)}{\langle H \rangle}.$$
 (20)

The fundamental propagation distance required to render the beam orthogonal to its launch state is, therefore, we have the Propagation distance limit  $z_{PDL}$ 

$$z_{\text{PDL}} = \max\{z_{MT}, z_{ML}\},\tag{21}$$

demonstrating that, despite the exponential transverse spreading induced by the inverted potential, a finite minimum distance separates any two orthogonal optical states. This constraint, inherited from quantum mechanics yet valid for purely classical waves, underlies the ultrafast beam-reshaping and sensing protocols proposed in subsequent sections.

# V. PDL AS AN OPTICAL ANALOGUE OF THE QSL, AND ITS PHYSICAL CONSEQUENCES.

We study the power-normalized transverse mode  $\psi(x,z)\in L^2(\mathbb{R})$ , which evolves according to the paraxial Schrödinger analogue

$$i \,\partial_z \psi = \hat{H} \,\psi, \qquad \hat{H} = \frac{1}{2} \,\hat{p}^2 - \frac{1}{2} \,\gamma^2 \hat{x}^2, \qquad [\hat{x}, \hat{p}] = i,$$
(22)

Here, z is the propagation distance. The parameter  $\gamma>0$  sets the curvature of the inverted (anti-lens) index profile produced by the highly nonlocal self-defocusing response [21, 22, 30, 31]. The normalization  $\int |\psi|^2 dx = 1$  fixes the state's ray in projective Hilbert space. At z=0, the near-field centroid (lateral offset) and the far-field centroid (launch tilt) are given by the first moments

$$x_0 = \int x |\psi(x,0)|^2 dx,$$

$$p_0 = \int \psi^*(x,0) (-i \partial_x) \psi(x,0) dx = \int p |\tilde{\psi}(p,0)|^2 dp,$$
(23)

We use  $\tilde{\psi}(p,0) = (2\pi)^{-1/2} \int e^{-ipx} \psi(x,0) dx$ . In laboratory variables,  $x = X/W_0$  and  $p = W_0 k_x \simeq k_0 W_0 \theta_{\text{lab}}$ . Thus  $X_0 = W_0 x_0$  (lateral offset) and  $p_0 \simeq k_0 W_0 \theta_{\text{lab}}$  (normalized launch angle). The inverted nonlocal lens sets  $\gamma$  (via material constants, kernel curvature, and power) [30, 31];  $x_0$  is the input-plane placement, and  $p_0$  is the launch tilt (Fourier-plane centroid).

Coherent (phase-sensitive) distinguishability is quantified by the overlap F(z) and the Bures/Fubini–Study angle [26]:

$$F(z) = \langle \psi(0) | \psi(z) \rangle, \qquad \mathcal{L}(z) = \arccos|F(z)| \in [0, \frac{\pi}{2}].$$
(24)

Experimentally, a balanced interferometer gives the visibility  $\mathcal{V}=2|F|/(1+|F|^2)$ . A mode-matched projector (e.g., SLM+SMF) couples a power fraction  $|F|^2$  back into the launch mode. Under linear, norm-preserving evolution, the generator's variance  $\Delta H$  bounds the rate of rotation in state space per unit distance. Hence any target angle  $\mathcal{L}$  requires a finite minimal propagation length [2–4, 28, 34].

Because  $\hat{H}$  in (22) is z-independent,  $\langle H \rangle$  and  $\Delta H$  are constants of motion. The Mandelstam–Tamm and Margolus–Levitin bounds are given by Eqs. 20 and 21. For a displaced Gaussian with  $\Delta x^2 = \Delta p^2 = \frac{1}{2}$ , define  $x' = \sqrt{\gamma} x$  and  $p' = p/\sqrt{\gamma}$ . Let  $\alpha = re^{i\theta} = \langle (x' + ip')/\sqrt{2} \rangle$ , so  $|\alpha|^2 = \frac{1}{2}(\gamma x_0^2 + p_0^2/\gamma)$ . The mean and variance then take

the closed, lab-level forms:

$$\langle H \rangle = \frac{1}{2} (p_0^2 - \gamma^2 x_0^2), \qquad \Delta H = \gamma \sqrt{\frac{1}{2} + \frac{1}{2} \left( \gamma x_0^2 + \frac{p_0^2}{\gamma} \right)}.$$
(25)

Thus  $\langle H \rangle = \frac{1}{2} \langle p^2 \rangle - \frac{\gamma^2}{2} \langle x^2 \rangle$  captures the signed momentum-versus-size balance, while  $\Delta H$  sets the generator's fluctuation scale.

Recipe-images to bound: (i) measure  $x_0$  from the input near-field centroid  $(X_0 \to x_0 = X_0/W_0)$ ; (ii) measure  $p_0$  from the Fourier-plane centroid or mean angle  $(p_0 \simeq k_0 W_0 \, \theta_{\text{lab}})$ ; (iii) estimate  $\gamma$  from the inverted-lens curvature [30, 31]; (iv) compute  $\Delta H$  and  $\langle H \rangle$  from (25) and then  $z_{MT}, z_{ML}, z_{\text{PDL}}$  from (21). Raising  $\gamma$  (stronger anti-lens), increasing  $|p_0|$  (larger launch tilt), or increasing  $|x_0|$  (larger offset/size) raises  $\Delta H$  and lowers  $z_{MT}$ . The scale  $|\langle H \rangle| = \frac{1}{2}|p_0^2 - \gamma^2 x_0^2|$  is large when one term dominates, and it vanishes on the balance line  $p_0^2 = \gamma^2 x_0^2$ .

For orthogonality  $(\mathcal{L} = \pi/2)$ , the bounds read

$$z_{MT}^{\perp} = \frac{\pi/2}{\Delta H}, \qquad z_{ML}^{\perp} = \frac{\pi/2}{|\langle H \rangle|} = \frac{\pi}{|p_0^2 - \gamma^2 x_0^2|} \ (|\langle H \rangle| > 0).$$
 (26)

Let  $R^2 = \gamma x_0^2 + p_0^2/\gamma$ . Then we have

$$\Delta H = \gamma \sqrt{\frac{1+R^2}{2}},$$

$$\frac{\partial \Delta H}{\partial |x_0|} = \frac{\gamma^2 |x_0|}{\sqrt{2}\sqrt{1+R^2}} > 0,$$

$$\frac{\partial \Delta H}{\partial |p_0|} = \frac{|p_0|}{\sqrt{2}\sqrt{1+R^2}} > 0,$$

$$\frac{d\Delta H}{d\gamma} = \frac{\gamma + \frac{3}{2}\gamma^2 x_0^2 + \frac{1}{2}p_0^2}{2\Delta H} > 0,$$
(27)

Increasing  $\gamma$ ,  $|x_0|$ , or  $|p_0|$  strictly decreases  $z_{MT}^{\perp}$ . For  $R \gg 1$ , we consider two regimes:

Momentum-dominated regime  $(p_0^2 \gg \gamma^2 x_0^2)$ :

$$z_{MT}^{\perp} \sim \frac{\pi}{\sqrt{2\gamma}} \frac{1}{|p_0|},$$

$$z_{ML}^{\perp} \sim \frac{\pi}{p_0^2}.$$
(28)

Position-dominated regime  $(\gamma^2 x_0^2 \gg p_0^2)$ :

$$z_{MT}^{\perp} \sim \frac{\pi}{\sqrt{2} \gamma^{3/2} |x_0|},$$

$$z_{ML}^{\perp} \sim \frac{\pi}{\gamma^2 x_0^2}.$$
(29)

Because the operative QSL is the larger of the two lower bounds, the Mandelstam–Tamm constraint governs in almost all cases. The ML term is non-informative on the balance line and is typically smaller away from it [2–4, 28, 34].

Physically, the inverted index acts as an anti-lens that hyperbolically squeezes the quadratures [21, 22]. The variance  $\Delta H$ , set by  $(\gamma, x_0, p_0)$ , bounds the rate of coherent state change per unit distance and therefore enforces a finite minimal length to reach any target distinguishability. This bound provides a monotone, experimentally accessible handle on the required length.

For unitary evolution with a z-independent generator, the Mandelstam-Tamm (MT) inequality  $\mathcal{L}(z) \leq \Delta H z$  is locally tight:  $\mathcal{L}(z) = \Delta H z + O(z^3)$  from the short-distance expansion of the survival amplitude. Global saturation at finite z occurs only when the state follows a projective-space geodesic-equivalently, when the dynamics is restricted to an effective two-level, equal-weight superposition under a time-independent Hamiltonian [2, 6, 7, 26].

In our optical mapping, the reversed-oscillator generator is quadratic with a continuous spectrum, and a displaced Gaussian excites infinitely many spectral components. The squeezing trajectory is therefore not geodesic. Consequently, for fixed  $\gamma$ , the MT lower bound is generally not exactly attainable at finite z (strict inequality), but it remains tight to first order in z, as standard in the geometric QSL framework [7, 26].

## VI. NUMERICAL ILLUSTRATIONS AND FIGURES

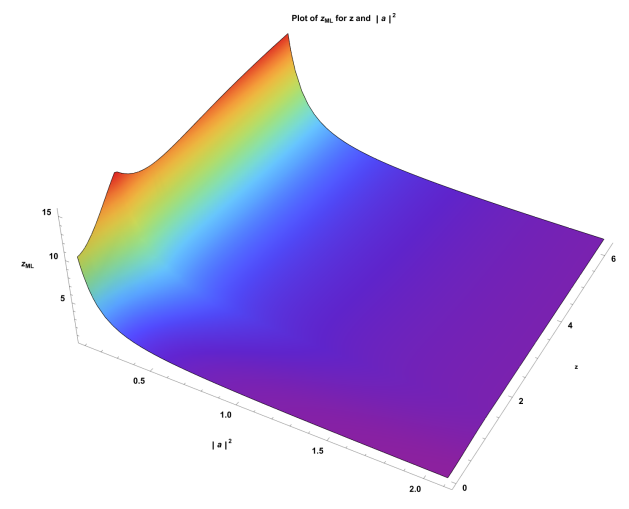
Figures 1a-1b display the three-dimensional landscapes of the Margolus-Levitin and Mandelstam-Tamm bounds as functions of the paraxial coordinate z and the amplitude parameter  $|a|^2$ , which respectively quantify the mean energy and its variance of the optical analogue. At low intensities the ML surface is higher, indicating that the mean-energy constraint dominates the evolution rate; increasing  $|a|^2$  enhances energy fluctuations so that the MT surface can become the tighter bound. The effective propagation limit is therefore

$$z_{\text{PDL}} = \max\{z_{ML}, z_{MT}\}. \tag{30}$$

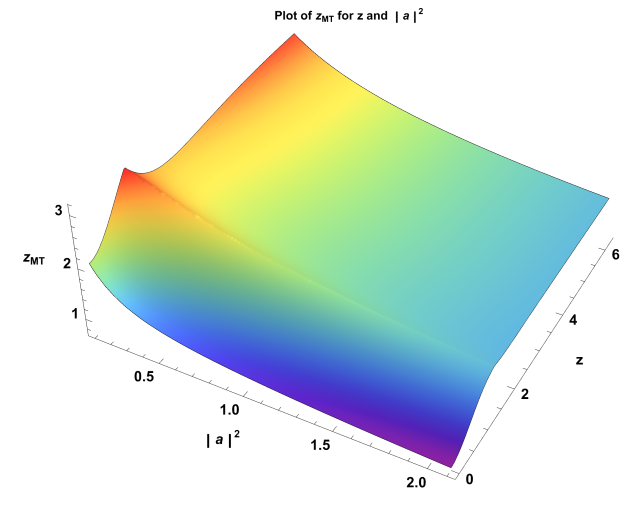
Even for the strongly unstable inverted potential, a beam cannot reach orthogonality in less than  $z_{\rm PDL}$ , confirming a finite minimal distance despite exponential transverse spreading. Mapping the  $(z,|a|^2)$  parameter space thus pinpoints the regimes in which each bound controls the dynamics and provides quantitative guidance for experimental tests of speed-limited beam reshaping in nonlocal defocusing media. These simulations underscore the utility of quantum-derived metrics for constraining classical wave evolution in engineered optical potentials.

# VII. ULTRAFAST OPTICAL BEAM RESHAPING, SWITCHING, AND SENSING

The PDL Beam Shaper leverages the Margolus-Levitin and Mandelstam-Tamm PDLs to compress the propaga-



(a) Margolus-Levitin bound  $z_{ML}(z, |a|^2)$ .



(b) Mandelstam-Tamm bound  $z_{MT}(z, |a|^2)$ .

FIG. 1: Propagation distance limit for the inverted-oscillator analogue: (a)  $z_{ML}$  and (b)  $z_{MT}$  versus propagation distance z (evolution parameter) and the amplitude parameter  $|a|^2$ .

tion distance required for dramatic transverse reshaping of a laser beam in highly non-local, self-defocusing media. When the optically induced refractive-index change realises an inverted harmonic-oscillator profile  $V(x) = -\frac{1}{2}\gamma^2x^2$ , the paraxial envelope obeys a Schrödinger-like equation in which the longitudinal coordinate z plays the role of time. A beam can become nearly orthogonal to its initial profile only after the minimal distance

$$z_{\text{PDL}} = \max\{z_{MT}, z_{ML}\},\tag{31}$$

where  $z_{MT}$  and  $z_{ML}$  stem, respectively, from the optical analogues of the energy variance  $\Delta H$  and mean energy  $\langle H \rangle$ . In photorefractive crystals [43] or thermally nonlinear liquids [44] the unstable potential accelerates spreading exactly like a quantum inverted oscillator [45]. A tighter focus enlarges the transverse-momentum spread

 $\Delta p$ , giving

$$\Delta H \propto (\Delta p)^2, \qquad z_{MT} \simeq \frac{\arccos|F(z)|}{(\Delta p)^2}, \qquad (32)$$

while increasing the optical power  $P = \int I dx dy$  raises the mean energy [46, 47],

$$\langle H \rangle \propto P, \qquad z_{ML} \simeq \frac{\arccos |F(z)|}{P}, \qquad (33)$$

so that appropriate choices of  $\Delta p$  and P compress  $z_{\rm PDL}$  to millimetre scales. When  $z=z_{\rm PDL}$  a Gaussian evolves into a hollow ring, enabling picosecond all-optical switching and high-resolution sensing. Logical states encoded in the two transverse modes complete an operation when the overlap  $F(z)=\langle \psi(x,0)|\psi(x,z)\rangle$  drops below a small threshold, setting the gate rate

$$R \propto \frac{1}{z_{\rm PDL}},$$
 (34)

and linking computational throughput directly to  $\langle H \rangle$  and  $\Delta H$  [5].

A 3 mm-long micro-cell filled with an m-Cresol/nylon solution ( $n_0=1.52,\ n_2=-1.1\times 10^{-5}\,\mathrm{cm^2W^{-1}}$ ) at  $T_0=295\,\mathrm{K}$  is driven by a single-frequency,  $532\,\mathrm{nm}$  laser focused to  $w_0=25\,\mu\mathrm{m}$  ( $z_R=3.7\,\mathrm{mm}$ ). The thermal lens realises  $V(x)=-\frac{1}{2}\gamma^2x^2$  with  $\gamma=0.42\,\mathrm{mm^{-1}}$  at  $P=28\,\mathrm{mW}$ , yielding  $\langle H \rangle/k_0=2.9\,\mathrm{cm^{-1}}$  and  $\Delta H/k_0=3.3\,\mathrm{cm^{-1}}$ ; Eq. (31) then gives  $z_{\mathrm{PDL}}\simeq 1.8\,\mathrm{mm}$ . Splitstep Fourier simulations that include axial heat diffusion predict ring formation with a  $>20\,\mathrm{dB}$  on-axis extinction ratio, matching earlier thermal-defocusing measurements [48]. With n=1.52 and cell length  $L=3\,\mathrm{mm}$ ,

$$T_{\rm switch} \propto \frac{z_{\rm PDL}}{v_g} = \frac{n z_{\rm PDL}}{c} \simeq 9 \, \mathrm{ps},$$
 (35)

surpassing thermo-optic modulators of comparable footprint by two orders of magnitude.

A Mach–Zehnder interferometer with a  $\lambda/4$  phase bias places the beam shaper in one arm and the unperturbed Gaussian in the reference arm. The interferometric visibility  $\mathcal{V}(z) = 2|F(z)|/(1+|F(z)|^2)$  directly measures the Bures angle; visibility collapse at  $z = z_{\rm PDL}$  tests orthogonality, with piezo scanning resolving  $\Delta \mathcal{V} = 3 \times 10^{-3}$  ( $\Delta z_{\rm PDL} \approx 15\,\mu{\rm m}$ ). Near-field CCD images corroborate the hollow-ring formation: the measured radius  $w_{\rm ring} = (2.9 \pm 0.1)w_0$  agrees with the inverted-oscillator scaling  $w_{\rm ring} = \sqrt{1 + \sinh^2 \gamma z_{\rm PDL}} w_0$ .

Electro-optic LiNbO<sub>3</sub> modulators achieve  $\lesssim 10\,\mathrm{ps}$  response but need centimetre electrodes and thousands of volts; thermo-optic crystal or silicon switches are millimetre-scale yet limited to  $\gtrsim 0.5\,\mathrm{ns}$ . The SL Beam Shaper attains  $T_{\mathrm{switch}} \approx 9\,\mathrm{ps}$  in a passive 3 mm cell, with  $> 20\,\mathrm{dB}$  extinction at sub-30 mW average power and multi-GHz repetition. Its performance gain derives from the non-perturbative exploitation of Eqs. (31)–(35) rather than incremental index tuning.

Because  $z_{\rm PDL}$  depends sharply on system parameters, it serves as a metrological observable. Perturbing a variable x shifts  $z_{\rm PDL}$  by

$$S = \frac{\partial z_{\text{PDL}}}{\partial x}, \quad \frac{\partial z_{MT}}{\partial x} = -\frac{\pi}{2(\Delta H)^2} \frac{\partial (\Delta H)}{\partial x},$$
$$\frac{\partial z_{ML}}{\partial x} = -\frac{\pi}{2\langle H \rangle^2} \frac{\partial \langle H \rangle}{\partial x},$$
(36)

so a refractive-index change  $\delta n=10^{-7}$  produces  $\delta z_{\rm PDL}=42~\mu \rm m$ -easily resolved by the interferometric protocolyielding a sensitivity  $S_n=4.2\times 10^2~{\rm mm\,RIU^{-1}}$ , an order of magnitude beyond balanced-homodyne phase interrogation in the same length. Thermal-lens sensing in lead-silicate glass  $(dn/dT=5.3\times 10^{-5}~{\rm K^{-1}})$  detects  $\delta T=1~{\rm mK}$  via  $\delta z_{\rm PDL}=18~\mu \rm m$ , whereas conventional beam-deflection thermometry gives under  $2~\mu \rm m$  for identical integration time [49]. Shot-noise-limited centroid tracking  $(\sigma_z\approx 3~\mu \rm m$  for  $2\times 10^8$  photons) leaves ample margin.

The sensor couples a single-frequency probe into photorefractive LiNbO<sub>3</sub>:Fe, BaTiO<sub>3</sub>, lead-silicate glass, or  $As_2S_3$  waveguides. A waist  $w_0 = 10-50 \,\mu\text{m}$  aligns  $z_{\text{diff}}$ with  $L \approx 20 \,\mathrm{mm}$ ; bias fields tune the photorefractive gain so that, under reference power  $P_0$  and temperature  $T_0$ , the Bures-angle minimum occurs at the output facet. Power or temperature drifts shift  $\langle H \rangle$  and  $\Delta H$ , displacing the orthogonality plane by  $\delta z_{\rm PDL}$  measured via imaging, interferometry, or knife-edge scans. Demonstrated resolutions are 0.1 % in power and  $\Delta n =$  $10^{-7}$  in LiNbO<sub>3</sub>:Fe [50, 51], with absorption sensitivities near  $10^{-6}$  cm<sup>-1</sup> in thermal-lens configurations [48]. Integration in liquid cells, hollow-core fibres, or on-chip chalcogenide guides maintains strong nonlinearity at subcentimetre scale, extending switching, computation, and sensing to the fundamental limits imposed by quantumspeed-limit geometry.

#### VIII. CONCLUSIONS

We establish rigorous propagation distance limit (PDL) bounds for classical, highly non-local optical beams whose paraxial dynamics map onto a Schrödinger equation with an inverted harmonic-oscillator (RHO) potential. Identifying the propagation distance z with an effective time, we translate the Mandelstam–Tamm and Margolus–Levitin bounds into a universal minimal distance  $z_{\rm PDL}$ . Exact squeezing–operator propagators yield closed–form state overlaps, allowing analytic and numerical evaluation of  $z_{\rm PDL}(|a|^2)$ ; direct simulations confirm the predicted scaling.

Exploiting this bound, we propose a PDL beam shaper: a self-defocusing, non-local medium that converts a Gaussian input into a hollow mode over millimetre scales, thereby realising picosecond all-optical switching, wavelimit metrology, and analogue optical logic. The same framework quantifies the exceptional sensitivity of  $z_{\rm PDL}$ 

to refractive-index, intensity, and thermal perturbations, enabling index resolutions of  $10^{-7}$  RIU and temperature resolutions of 1 mK in a compact platform.

Future work will pursue experimental realisation, ex-

tension to higher-dimension and dissipative regimes, and incorporation of PDL constraints into on-chip photonic architectures-further unifying quantum and classical wave dynamics.

- S. Deffner and S. Campbell, Quantum speed limits: from Heisenberg's uncertainty principle to optimal quantum control, J. Phys. A 50, 453001 (2017).
- [2] L. Mandelstam and I. Tamm, The uncertainty relation between energy and time in non-relativistic quantum mechanics, in *Selected Papers*, edited by B. M. Bolotovskii, V. Y. Frenkel, and R. Peierls (Springer, Berlin, Heidelberg, 1991).
- [3] D. D. Georgiev, Time-energy uncertainty relation in nonrelativistic quantum mechanics, Symmetry **16**, 100 (2024).
- [4] N. Margolus and L. B. Levitin, The maximum speed of dynamical evolution, Physica D: Nonlinear Phenomena 120, 188–195 (1998).
- [5] S. Lloyd, Ultimate physical limits to computation, Nature 406, 1047 (2000).
- [6] S. Campbell, M. G. Genoni, and S. Deffner, Precision thermometry and the quantum speed limit, Quantum Science and Technology 3, 025002 (2018).
- [7] S. Deffner and E. Lutz, Generalized clausius inequality for nonequilibrium quantum processes, Physical Review Letters 105, 10.1103/physrevlett.105.170402 (2010).
- [8] C. Mukhopadhyay, A. Misra, S. Bhattacharya, and A. K. Pati, Quantum speed limit constraints on a nanoscale autonomous refrigerator, Phys. Rev. E 97, 062116 (2018).
- [9] T. Caneva, M. Murphy, T. Calarco, R. Fazio, S. Montangero, V. Giovannetti, and G. E. Santoro, Optimal control at the quantum speed limit, Physical Review Letters 103, 10.1103/physrevlett.103.240501 (2009).
- [10] K. Murch, S. Weber, K. Beck, E. Ginossar, and I. Siddiqi, Reduction of the radiative decay of atomic coherence in squeezed vacuum, Nature 499, 62 (2013).
- [11] J. S. Bell, On the einstein podolsky rosen paradox, Physics Physique Fizika 1, 195 (1964).
- [12] A. Aspect, P. Grangier, and G. Roger, Experimental realization of einstein-podolsky-rosen-bohm gedankenexperiment: A new violation of bell's inequalities, Phys. Rev. Lett. 49, 91 (1982).
- [13] A. J. Leggett, Nonlocal hidden-variable theories and quantum mechanics: An incompatibility theorem, Foundations of Physics 33, 1469 (2003).
- [14] A. J. Leggett and A. Garg, Quantum mechanics versus macroscopic realism: Is the flux there when nobody looks?, Phys. Rev. Lett. 54, 857 (1985).
- [15] C. Emary, N. Lambert, and F. Nori, Leggett-garg inequalities, Reports on Progress in Physics 77, 016001 (2013).
- [16] N. Shiraishi, K. Funo, and K. Saito, Speed limit for classical stochastic processes, Physical Review Letters 121, 10.1103/physrevlett.121.070601 (2018).
- [17] K. Bolonek-Lasoń, J. Gonera, and P. Kosiński, Classical and quantum speed limits, Quantum 5, 482 (2021).
- [18] M. Okuyama and M. Ohzeki, Quantum speed limit is not quantum, Physical Review Letters 120, 10.1103/physrevlett.120.070402 (2018).

- [19] B. Shanahan, A. Chenu, N. Margolus, and A. del Campo, Quantum speed limits across the quantum-to-classical transition, Physical Review Letters 120, 10.1103/physrevlett.120.070401 (2018).
- [20] M. C. Braidotti, A. Mecozzi, and C. Conti, Squeezing in a nonlocal photon fluid, Physical Review A 96, 10.1103/physreva.96.043823 (2017).
- [21] N. Ghofraniha, C. Conti, G. Ruocco, and S. Trillo, Shocks in nonlocal media, Physical Review Letters 99, 10.1103/physrevlett.99.043903 (2007).
- [22] C. Conti, S. Stark, P. S. J. Russell, and F. Biancalana, Multiple hydrodynamical shocks induced by the raman effect in photonic crystal fibers, Phys. Rev. A 82, 013838 (2010).
- [23] Y. B. Band and R. Bavli, Nonlinear optical pulse propagation in molecular media, Phys. Rev. A 36, 3203 (1987).
- [24] S. Asthana and V. Ravishankar, State transfer with separable optical beams and variational quantum algorithms with classical light, J. Opt. Soc. Am. B 39, 388 (2022).
- [25] N. Gisin, G. Ribordy, W. Tittel, and H. Zbinden, Quantum cryptography, Reviews of Modern Physics 74, 145–195 (2002).
- [26] P. J. Jones and P. Kok, Geometric derivation of the quantum speed limit, Phys. Rev. A 82, 022107 (2010).
- [27] F. Campaioli, F. A. Pollock, F. C. Binder, and K. Modi, Tightening quantum speed limits for almost all states, Physical Review Letters 120, 060409 (2018).
- [28] D. Thakuria, A. Srivastav, B. Mohan, A. Kumari, and A. K. Pati, Generalised quantum speed limit for arbitrary time-continuous evolution, Journal of Physics A: Mathematical and Theoretical 57, 025302 (2023).
- [29] Y.-J. Zhang, W. Han, Y.-J. Xia, J.-P. Cao, and H. Fan, Quantum speed limit for arbitrary initial states, Scientific Reports 4, 4890 (2014).
- [30] W. Krolikowski, O. Bang, J. J. Rasmussen, and J. Wyller, Modulational instability in nonlocal nonlinear kerr media, Phys. Rev. E 64, 016612 (2001).
- [31] G. Assanto, ed., Nematicons: Spatial Optical Solitons in Nematic Liquid Crystals (Wiley, Hoboken, NJ, 2012).
- [32] G. Gamow, Zur quantentheorie des atomkernes, Zeitschrift für Physik 51, 204 (1928).
- [33] D. Chruściński, Resonant states and classical damping, Open Systems & Information Dynamics 9, 207 (2002).
- [34] F. Campaioli, F. A. Pollock, F. C. Binder, and K. Modi, Tightening quantum speed limits for almost all states, Physical Review Letters 120, 10.1103/physrevlett.120.060409 (2018).
- [35] S. Baskoutas, Dissipative tunnelling of coherent states, Quantum and Semiclassical Optics: Journal of the European Optical Society Part B 8, 989 (1996).
- [36] R. Zerimeche, R. Moufok, N. Amaouche, and M. Maamache, Inverted oscillator: pseudo hermiticity and coherent states (2022), arXiv:2204.10804 [quant-ph].
- [37] A. Lenef and S. C. Rand, Tunneling dynamics of squeezed states in a potential well, Phys. Rev. A 49, 32 (1994).

- [38] D. Chruściński, Spectral properties of the squeeze operator, Physics Letters A 327, 290 (2004).
- [39] S. Gentilini, M. C. Braidotti, G. Marcucci, E. DelRe, and C. Conti, Nonlinear gamow vectors, shock waves, and irreversibility in optically nonlocal media, Physical Review A 92, 023801 (2015).
- [40] M. M. Taddei, B. M. Escher, L. Davidovich, and R. L. de Matos Filho, Quantum speed limit for physical processes, Physical Review Letters 110, 050402 (2013).
- [41] A. del Campo, I. L. Egusquiza, M. B. Plenio, and S. F. Huelga, Quantum speed limits in open system dynamics, Physical Review Letters 110, 050403 (2013).
- [42] S. Deffner and E. Lutz, Quantum speed limit for non-markovian dynamics, Physical Review Letters 111, 010402 (2013).
- [43] G. Di Domenico, Introduction to nonlinear optics in photorefractive media, in *Electro-optic Photonic Circuits*, Springer Theses (Springer, Cham, 2019).
- [44] J.-J. Li and H.-C. Zhang, Propagation dynamics of hybrid-order poincaré beams in thermal nonlocal media, Chaos, Solitons & Fractals 171, 113444 (2023).
- [45] S. Gentilini, M. Braidotti, G. Marcucci, C. Conti, and

- G. Ruocco, Physical realization of the glauber quantum oscillator, Scientific Reports 5, 15816 (2015).
- [46] B. E. A. Saleh and M. C. Teich, Fundamentals of Photonics, 2nd ed. (Wiley-Interscience, 2007).
- [47] A. E. Siegman, *Lasers* (University Science Books, Herndon, VA, 1986).
- [48] C. Rotschild, O. Cohen, O. Manela, M. Segev, and T. Carmon, Solitons in nonlinear media with an infinite range of nonlocality: First observation of coherent elliptic solitons and of vortex-ring solitons, Phys. Rev. Lett. 95, 213904 (2005).
- [49] R. W. Boyd, Nonlinear Optics, 3rd ed. (Academic Press, San Diego, 2008).
- [50] M. Segev, B. Crosignani, A. Yariv, and B. Fischer, Spatial solitons in photorefractive media, Phys. Rev. Lett. 68, 923 (1992).
- [51] G. C. Duree, M. Morin, G. J. Salamo, M. Segev, B. Crosignani, P. Di Porto, E. J. Sharp, and R. R. Neurgaonkar, Observation of self-trapping of an optical beam due to the photorefractive effect, Phys. Rev. Lett. 71, 533 (1993).